Journal of Materials Chemistry C

ROYAL SOCIETY OF CHEMISTRY

PAPER

View Article Online
View Journal

Cite this: DOI: 10.1039/d0tc05903j

The role of fullerene derivatives in perovskite solar cells: electron transporting or electron extraction layers?†

Olivia Fernandez-Delgado, ‡[a] P. S. Chandrasekhar, ‡[ab] Natalia Cano-Sampaio, [ac] Zoe C. Simon, [d] Alain R. Puente-Santiago, [a] Fang Liu,[e] Edison Castro [d] and Luis Echegoyen *[a]

The synthesis, characterization and incorporation of fullerene derivatives bearing primary, secondary and tertiary nitrogen atoms, which possess different basicities, in perovskite solar cells (PSCs), is reported. In this work, we tested the compounds as conventional electron transporting materials (ETMs) in a single layer with phenyl-C_{61}-butyric acid methyl ester ($PC_{61}BM$) as control. Additionally, we tested the idea of separating the ETM into two different layers: a thin electron extracting layer (EEL) at the interface with the perovskite, and an electron transporting layer (ETL) to transport the electrons to the Ag electrode. The compounds in this work were also tested as EELs with C_{60} as ETL on top. Our results show that the new fullerenes perform better as EELs than as ETMs. A maximum power conversion efficiency (PCE) value of 18.88% was obtained for a device where a thin layer (~3 nm) of BPy-C_{60} was used as EEL, a higher value than that of the control device (16.70%) with only pure C_{60}. Increasing the layer thicknesses led to dramatically decreased PCE values, clearly proving that the compound is an excellent electron extractor from the perovskite layer but a poor transporter as a bulk material. The improved passivation ability and electron extraction capabilities of the BPy-C_{60} derivative were demonstrated by steady state and time-resolved photoluminescence (SS-and TRPL) as well as electrochemical impedance spectroscopy (EIS) and X-Ray photoelectron spectroscopy (XPS) measurements; likely attributed to the enhanced basicity of the pyridine groups that contributes to a stronger interaction with the interfacial Pb^{2+}.

Received 16th December 2020,
Accepted 9th February 2021

DOI: 10.1039/d0tc05903j

rsc.li/materials-c

Introduction

During the last decade, PSCs have received considerable attention in the field of new generation photovoltaics, with measured PCE values above 25%.[1] This remarkable progress is attributed to the excellent light absorption coefficients (~105 cm^{-1}),[2,3] tunable optoelectronic properties,[4–6] high defect tolerance[7,8] and long carrier diffusion lengths in films (>175 μm).[9–11] However, before they can go to market and compete with the commercially available silicon solar cells,[12,13] their stability under ambient working conditions needs to be improved.

Perovskite films are usually polycrystalline, possessing many imperfections, such as grain boundaries, pinholes and crystallographic defects.[14,15] These defects are mostly found at the surfaces; thus, their passivation is crucial to inhibit electron–hole recombination and to increase efficiencies.[16–18] Several efficient passivation methods are based on the charged nature of the perovskite surface and use ETMs that contain either Lewis bases (thiophene, pyridine, carboxylate, phosphate) or Lewis acid groups to passivate these defects *via* coordination or electrostatic interactions.[17,19]

To date, PSCs are being fabricated predominantly using two device configurations: regular n–i–p structures in which ITO or FTO transparent conducting glass acts as the cathode, and inverted p–i–n structures in which the FTO or ITO glass acts as the anode.[20–22] In the p–i–n configuration, fullerenes and their derivatives such as PC_xBMs; x = 61 or 71, are widely used as ETMs, owing to their superior charge carrier extraction ability, low temperature solution processing, and excellent solubility.[23–26] Fullerene C_{60}, C_{70}, and their derivatives have

[a] Department of Chemistry and Biochemistry, University of Texas at El Paso, 500 West University Avenue, El Paso, TX, 79968, USA. E-mail: echegoyen@utep.edu
[b] Conn Center for Renewable Energy Research, University of Louisville, 216 Eastern parkway, Louisville, KY 40292, USA
[c] Department of Chemistry, Universidad del Valle, 13 St. Cali, Valle del Cauca, Colombia
[d] Department of Chemistry, University of Pittsburgh, Pittsburgh, Pennsylvania 15260, USA
[e] Department of Chemistry, Columbia University, New York, NY, 10027, USA

† Electronic supplementary information (ESI) available. See DOI: 10.1039/d0tc05903j

‡ These authors contributed equally.

been extensively employed to enhance device efficiency by improving the open circuit voltage (V_{oc}), fill factor (FF) and by reducing photocurrent hysteresis.[27–30] Several studies have reported the use of bathocuproine (BCP), Ca, lithium fluoride (LiF), polyethylenimine ethoxylated (PEIE), and fullerene (C_{60}-bis) to improve the ohmic contact and to reduce the interface barrier to electron extraction between the ETM and the top metal contact resulting in an enhanced PSC performance.[31–34] Furthermore, fullerene derivatives such as DMAPA-C_{60} and PCBB-2CN-2C8 have been successfully incorporated as interfacial layers for improving the PSCs' response by enhancing charge transport and minimizing recombination losses.[35] In the p–i–n configuration, both hole and electron transport layers play a vital role in the extraction of charge carriers. PEDOT:PSS is a widely used hole transport layer in p–i–n PSCs, but it limits the PCE and stability of PSCs due to its hygroscopic and acidic nature. Hence, the introduction of additives and modification of PEDOT:PSS has been widely explored for improving the PCE of PSCs. For instance, sodium benzenesulfonate (SBS) has been applied to modify the PEDOT:PSS (SBS–PEDOT:PSS) layer to obtain a smoother surface and better energy-level alignment with the perovskite layer. This has resulted in improved of PCEs from 18.07% to 19.41%.[36] Z. Zhang *et al.*, introduced an ultrathin PTAA layer between the PEDOT:PSS and the active perovskite layer to improve hole transfer by suppressing the interfacial recombination, which resulted in a PCE of 19% and a FF of 82.59%.[37] A modified one-step spin coating method was introduced using a methyl ammonium iodide (MAI) layer spun over the top of PEDOT:PSS to improve hole extraction by obtaining the optimum iodide concentration gradient. A similar approach using methyl ammonium chloride (MACl) was applied over the SnO_2 ETL to passivate the grain boundary defects to prevent perovskite degradation and to improve the charge carrier extraction and transport.[38,39] Additionally, (4-(1,3-dimethyl-2,3-dihydro-1*H*-benzoimidazol-2-yl)phenyl) dimethylamine (*n*-DMBI) has been used as a dopant in the ETM layer to achieve high PCEs and thermal stability by increasing electrical conductivity, electron mobility, and charge extraction ability of ETM layer.[40]

On the other hand, the thickness of the interfacial layer plays an important role for obtaining high PCE values.[41,42] Therefore, it is crucial to prepare optimal thicknesses of the interlayer to facilitate electron extraction at those interfaces. To the best of our knowledge, there are no reports that describe the effect and optimization of the thicknesses of interfacial fullerene layers when used either as EELs or as ETMs. Here, we report the synthesis, characterization and the effect of different nitrogen containing fullerene derivatives when incorporated as ETM single layer or thin EEL in PSCs. We wanted to experimentally establish the intrinsic abilities of EEL compounds and separate this capability from their bulk electron transporting properties.

Results and discussion

In this work, we not only studied the effects of the fullerene substituents on the device performances, we also determined the optimal conditions to obtain the best performing devices when the fullerenes were used either as ETM single layers or as thin EELs in an effort to understand their intrinsic electron extraction vs transport abilities. Normally, fullerenes in these kinds of devices are used generically as ETMs, but here, we subdivide the process as: extraction at the interface, performed by the EEL and transportation in the bulk performed by the ETL, to test the differential ability of the compounds to act as ETL and EEL. The fullerene derivatives reported in this study (Fig. 2) were designed to have, in each case, a nitrogen atom with different basicity, to study how this affects the interfacial interactions with the perovskite layer. It is very well known, as shown in Fig. 1 that the basicity of the different nitrogen types follows the order: pyridine > aniline > carbamate.[43,44]

The fullerene derivatives (BPy-C_{60},[45] BAn-C_{60}, and BpAn-C_{60}) were prepared by a Bingel–Hirsch reaction in relatively high yields (93%, 90% and 75%, respectively). The synthetic details are described in the ESI.†

The electrochemical properties of the new derivatives were investigated by cyclic voltammetry (CV). The measurements were recorded using *ortho*-dichlorobenzene (*o*-DCB) as solvent, and a 0.1 M of *n*-Bu_4NPF_6 as the electrolyte; a 1 mm glassy carbon electrode was used as the working electrode, a silver wire as pseudo-reference and a platinum wire as the counter electrode. All compounds exhibited three well defined chemically reversible and electrochemically quasi reversible reduction waves. UV-Vis was performed to study their optoelectronic properties, showing that all derivatives displayed similar absorption spectra, with bands located at 344.6, 427.7 and 487.8 nm, as expected for C_{60} *mono*-adducts. The absorption onset (λ_{abs}) was estimated from the UV-Vis spectra (Fig. 3b, eqn (1)), and the reduction potential onset (E^{on}_{red}) was obtained from the CV measurements (Fig. 3a). The lowest unoccupied molecular orbital (LUMO) values were calculated using eqn (2),[46] and the highest occupied molecular orbital (HOMO) values for the compounds were calculated by eqn (3). Table 1 summarizes all the values corresponding to the energy levels (Fig. 3c), optical bandgaps (E_g) and E^{on}_{red} of the fullerene derivatives.[47]

$$E_g = 1242/\lambda_{abs}\ (\text{eV}) \quad (1)$$

$$\text{LUMO} = -e(E^{on}_{red} + 4.8)\ (\text{eV}) \quad (2)$$

$$\text{HOMO} = \text{LUMO} - E_g\ (\text{eV}) \quad (3)$$

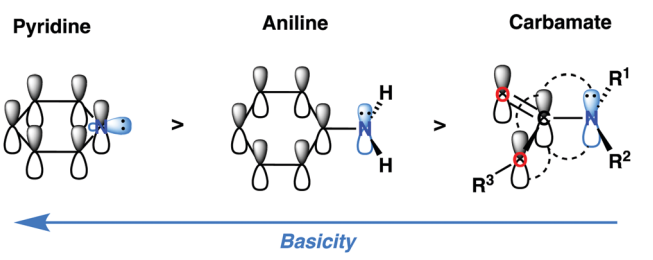

Fig. 1 Orbital representation of pyridine, aniline and carbamate.

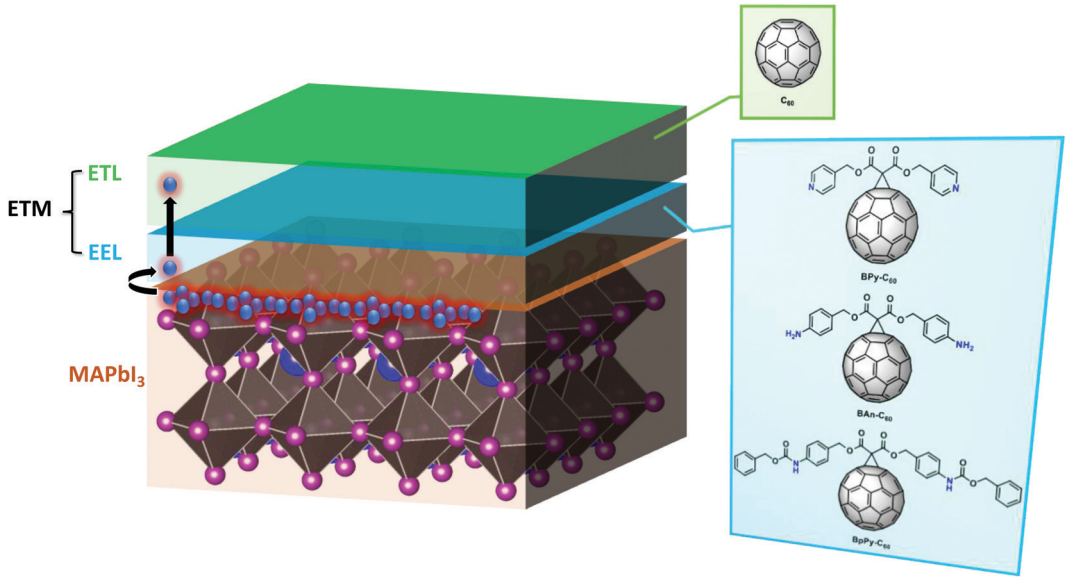

Fig. 2 (a) Device structure with the fullerene C_{60}, BPy-C_{60}, BAn-C_{60} and BpAn-C_{60} used as ETM, EEL and ETL.

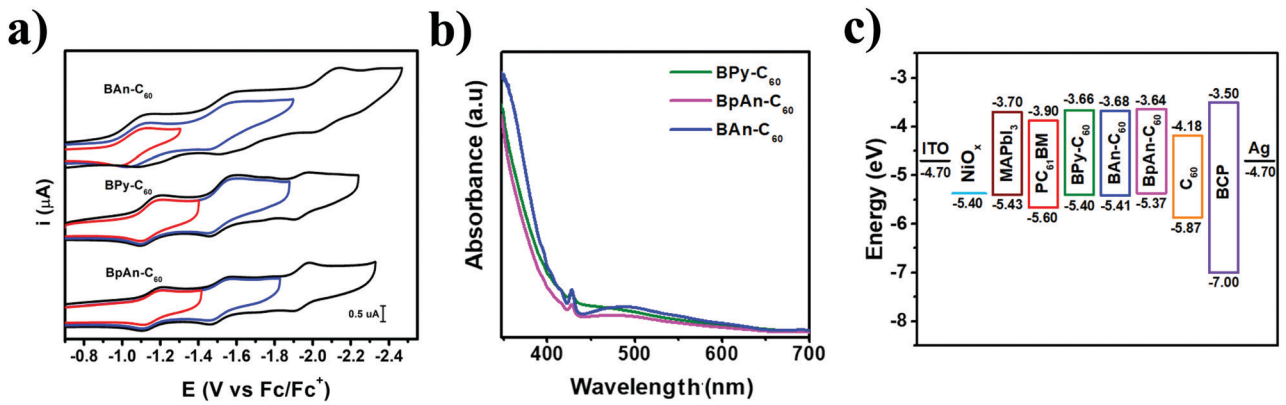

Fig. 3 (a) Cyclic voltammetry, (b) UV-Vis and (c) energy level diagram for the compounds BPy-C_{60}, BAn-C_{60} and BpAn-C_{60}.

Table 1 Energy levels, the first reduction onset, UV-Vis absorption onset and optical bandgap of BPy-C_{60}, BAn-C_{60}, and BpAn-C_{60}

Compound	λ_{abs} (nm)	E_g (eV)	E_{red}^{on} (V)	LUMO (eV)	HOMO (eV)
$PC_{61}BM$[a]	695	1.78	−0.92	−3.88	−5.66
BPy-C_{60}	714	1.74	−1.14	−3.66	−5.40
BAn-C_{60}	716	1.73	−1.12	−3.68	−5.41
BpAn-C_{60}	717	1.73	−1.16	−3.64	−5.37

[a] Values from ref. 46.

By comparing the energy levels of the synthesized compounds to those for the perovskite (Fig. 3c), it is observed that the LUMO matches the conduction band of the perovskite, thus allowing the transport of electrons to the Ag electrode. The HOMO matches the valence band of the perovskite to block the transport of holes, thus, allowing an efficient charge separation.

The structural and morphological characterization of the perovskite film were performed by scanning electron microscopy (SEM) and X-Ray Diffraction (XRD). Surface SEM (Fig. 4a) shows perovskite surfaces that are homogeneous, with no apparent pinholes and with an average grain size of approximately 300 nm. Cross-section SEM (Fig. 4b) for a device constructed with $PC_{61}BM$ as ETM displays the morphology of all layers that compose a typical device with the following architecture: commercially acquired ITO (~100 nm) on glass, the compact NiO_x layer (~25 nm) used as HTM, the perovskite

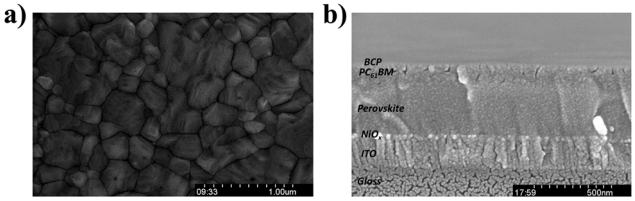

Fig. 4 (a) SEM of the perovskite surface, (b) cross-section SEM to the general device architecture.

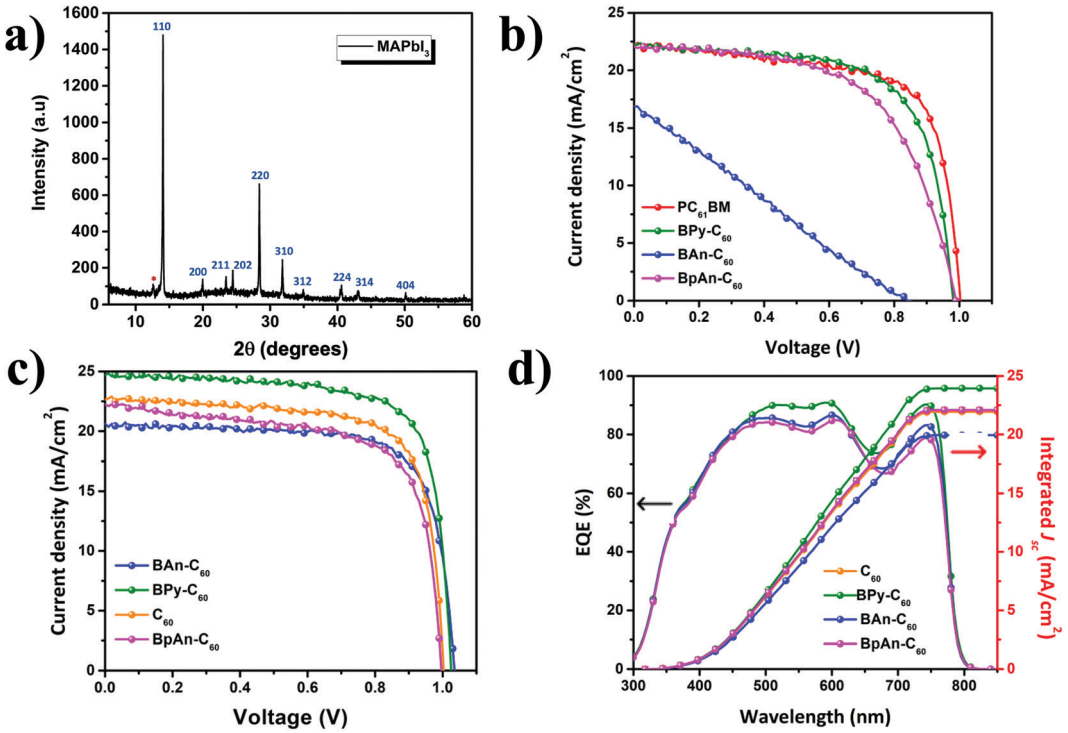

Fig. 5 (a) XRD characterization of the perovskite, (b) *J–V* curves of devices with the new compounds used as ETM, (c) *J–V* curves and (d) EQE for the devices with the new compounds used as EEL.

active layer (~350 nm) followed by the ETM (~85 nm) and lastly a BCP (~20 nm) thin layer. All the thicknesses were estimated by SEM.

XRD measurements (Fig. 5a) revealed the high crystallinity of the perovskite layer, given by a preferential growth in the 110 plane, evidenced by a high intensity peak at 14.5°. Other characteristic peaks of the typical tetragonal phase were also observed at 20.0°, 23.8°, 24.9°, 28.0°, 31.5°, 35.0°, 41.0°, 42.6,° and 50.0°.[48]

As mentioned above, devices with an inverted architecture (glass/ITO/NiO_x/perovskite/fullerene/BCP/Ag) were constructed using the fullerene derivatives as ETM with $PC_{61}BM$ as the control. The *J–V* characteristics of those devices are shown in Fig. 5b. The best performance was observed with the device containing BPy-C_{60} fullerene derivative; and the devices based on the other compounds exhibited a rather poor performance as ETM when compared to $PC_{61}BM$ (Table 2).

The space charge limited current (SCLC) method was used in electron-only devices with the structure ITO/Cs_2CO_3/fullerene/Ag measured under dark ambient conditions to calculate the electron mobilities (μ) (ESI,† Fig. S1 and Table S1) to study the electron transport properties of the fullerenes in the bulk. The results showed that all the compounds had a smaller value of μ compared to C_{60} (6.21×10^{-4} cm^2 V^{-1} s^{-1}) and $PC_{61}BM$ (5.74×10^{-4} cm^2 V^{-1} s^{-1}), being 1.22×10^{-4} cm^2 V^{-1} s^{-1}, 1.15×10^{-4} cm^2 V^{-1} s^{-1} and 9.29×10^{-5} cm^2 V^{-1} s^{-1} for BPy-C_{60}, BpAn-C_{60}, and BAn-C_{60}, respectively. This result explains why the compounds exhibited a poor performance in devices using them as ETM.

Table 2 Photovoltaic parameters of PSCs using different ETMs

Compound	V_{oc} (V)	J_{sc} (mA cm^{-2})	FF (%)	PCE (%)
$PC_{61}BM$	1.033 ± 0.002	22.05 ± 0.49	70 ± 1	15.43 ± 0.92
BPy-C_{60}	0.980 ± 0.004	22.31 ± 0.19	67 ± 1	14.59 ± 0.21
BpAn-C_{60}	0.989 ± 0.013	22.05 ± 0.38	59 ± 2	12.92 ± 0.24
BAn-C_{60}	0.851 ± 0.008	16.93 ± 0.76	24 ± 1	3.42 ± 0.21

To differentiate their electron transport from their electron extraction abilities, the fullerene derivatives were tested as interfacial layers between the perovskite and C_{60} acting as ETL, since the latter is an excellent transporter, but not optimal for extracting electrons at the interface. The optimal electron extraction conditions were obtained by tuning the thicknesses of the EEL, followed by the addition of a C_{60} layer for a total layer thickness of 85 nm. C_{60} was introduced to help with the transport of the electrons to the Ag electrode once extracted at the interface by the EELs.

As shown in Table 3, as the thickness of the EEL decreased, the devices' performances increased monotonically, which shows that the compounds are efficient at extracting the electrons from the perovskite interface, but do not perform well when transporting them to the electrode. The results for the *J–V* characteristics and external quantum efficiency (EQE) are shown in Fig. 5c and d and are summarized in Table 3.

The best performing device containing BPy-C_{60} was the one with a 3 nm EEL. In this case, an increment of the J_{sc} and FF was observed, which can be attributed to an enhanced interfacial contact between the layers as well as passivation of the

Table 3 Photovoltaic parameters of different fullerene derivatives as EELs as a function of its thickness and C_{60} as ETL

Compound	Thickness (nm)	V_{oc} (V)	J_{sc} (mA cm^{-2})	FF (%)	PCE (%)
Pure C_{60}	85 ± 2	1.033 ± 0.004	22.80 ± 0.68	73 ± 1	16.70 ± 0.84
Pure BPy-C_{60}	85 ± 3	0.980 ± 0.004	22.31 ± 0.19	67 ± 1	14.59 ± 0.21
BPy-C_{60} + C_{60} (total thickness 85 nm)	3 ± 1	1.025 ± 0.005	24.70 ± 0.11	75 ± 1	18.88 ± 0.18
	5 ± 2	0.989 ± 0.009	22.14 ± 0.20	69 ± 3	15.14 ± 0.21
	10 ± 3	0.981 ± 0.023	20.12 ± 0.69	65 ± 2	12.82 ± 0.32
	20 ± 2	0.975 ± 0.019	18.92 ± 0.84	59 ± 2	10.88 ± 0.65
Pure BpAn-C_{60}	85 ± 3	0.989 ± 0.013	22.05 ± 0.38	59 ± 2	12.92 ± 0.24
BpAn-C_{60} + C_{60} (total thickness 85 nm)	3 ± 1	0.996 ± 0.013	22.24 ± 0.38	69 ± 2	15.21 ± 0.28
	5 ± 2	0.986 ± 0.006	22.05 ± 0.43	59 ± 1	12.92 ± 0.43
	10 ± 3	0.963 ± 0.032	21.80 ± 0.86	55 ± 1	11.53 ± 0.19
	20 ± 2	0.954 ± 0.054	18.98 ± 1.12	51 ± 2	9.23 ± 0.38
Pure BAn-C_{60}	85 ± 2	0.851 ± 0.008	16.93 ± 0.76	24 ± 1	3.42 ± 0.21
BAn-C_{60} + C_{60} (total thickness 85 nm)	3 ± 2	1.035 ± 0.008	20.65 ± 0.89	73 ± 1	15.70 ± 0.19
	5 ± 2	0.991 ± 0.014	19.81 ± 0.32	69 ± 1	13.54 ± 0.18
	10 ± 3	0.983 ± 0.009	18.92 ± 0.54	63 ± 2	11.71 ± 0.32
	20 ± 2	0.979 ± 0.021	18.11 ± 0.62	59 ± 3	10.46 ± 0.39

perovskite grain boundaries. The devices based on the other compounds performed similar to the control device using only C_{60} as ETM. The thinner the EEL, the better the performance of the devices.

A statistical analysis of the obtained photovoltaic parameters was carried out (Fig. S3, ESI†) and the reproducibility of the methodology employed was confirmed. Additionally, a comparative stability study was performed with devices fabricated with the best performing compound (BPy-C_{60}) and C_{60} as control (Fig. S4, ESI†), which exhibited an increased stability under ambient conditions (without encapsulation, 50% humidity) for the devices based on the new derivative.

To further investigate the effect of the different fullerene derivatives on the interfacial passivation and electron extraction processes, SS-and TRPL were performed. All the fullerene derivatives and $PC_{61}BM$, used as control, were spun coated on a perovskite layer to study their passivation effects. As shown in Fig. 6, BPy-C_{60} shows a more efficient quenching of the photoluminescence, in agreement with the photovoltaic results. This effect is related to the strong interaction that pyridine has with the uncoordinated Pb^{2+} at the interface, which prevents the electron/hole recombination, resulting in a decrease of the photoluminescence signal. In the case of the other compounds, they are also able to passivate the perovskite surface to some degree, probably driven by interfacial interactions *via* carbonyl, carbamate or amino groups.

TRPL was also measured by monitoring the emission peaks of the perovskite with time to explore the electron extraction properties of all compounds. The decay curves were fitted with a bi-exponential function and the fast (τ_1) and slow (τ_2) decay domains were calculated and are presented in Table 4. As shown in Fig. 6b, BPy-C_{60} exhibits a much faster decay compared to the other derivatives, which is in agreement with our hypothesis based on the enhanced electron extraction ability of BPy-C_{60}.

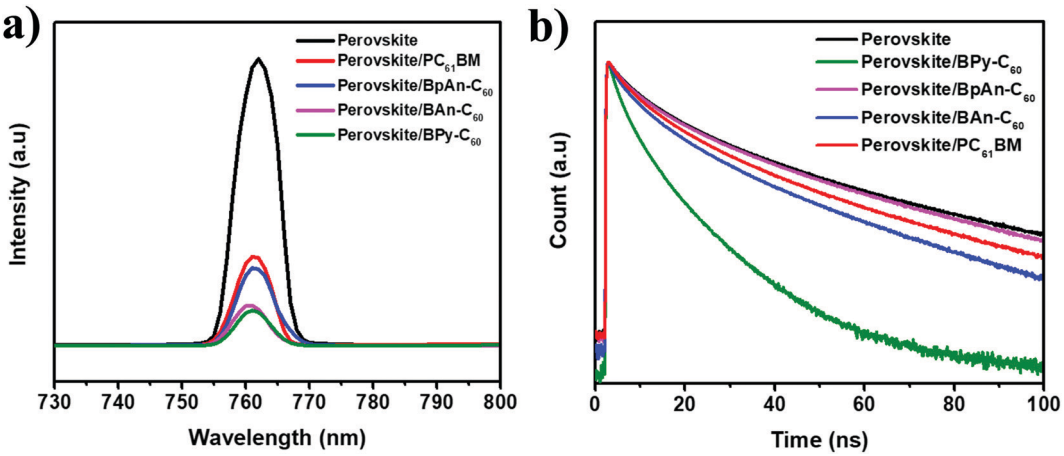

Fig. 6 (a) SS and (b) TRPL for devices constructed as $MAPbI_3$/fullerene derivatives.

Table 4 Carrier lifetime for $MAPbI_3$ and $MAPbI_3$/fullerene films

Compound	τ_1 (ns)	τ_2 (ns)
Perovskite	97.5	202.4
Perovskite/$PC_{61}BM$	88.7	93.6
Perovskite/BPy-C_{60}	23.5	35.9
Perovskite/BpAn-C_{60}	91.3	88.9
Perovskite/BAn-C_{60}	87.2	94.6

Conductivity measurements were carried out (ESI,† Fig. S2 and Table S2) and the results confirmed that the compounds have similar values of conductivity: 6.32×10^{-3} S cm^{-1}, 4.86×10^{-3} S cm^{-1}, 5.24×10^{-3} S cm^{-1} for BPy-C_{60}, BAn-C_{60}, and BpAn-C_{60} respectively, which are slightly higher than the one for $PC_{61}BM$ (1.12×10^{-4} S cm^{-1}). In the case of C_{60}, the device exhibited a conductivity of 5.86×10^{-3} S cm^{-1}, in agreement with the PCE values obtained for the devices with the fullerene compounds as EELs. Considering that conductivity is directly proportional to the product of carrier concentration and electron mobility, the previously described values support the idea that the compounds exhibit an enhanced electron extraction capability when compared to $PC_{61}BM$, rather than the transport of electrons in bulk. For BPy-C_{60}, an increased ability to extract electrons compared to C_{60} and the other fullerene derivatives results in an enhanced photovoltaic performance.

To further examine the passivation processes, XPS measurements were conducted (Fig. 7a). The results revealed that all the synthesized fullerenes induce a shift in the $4f_{7/2}$ and $4f_{5/2}$ orbitals of Pb^{2+} compared to the pure perovskite, which has a binding energy of 137.98 eV and 142.86 eV, respectively. Additionally, BPy-C_{60} shows the most prominent shift for the $4f_{7/2}$ and $4f_{5/2}$ binding energy of 0.42 eV (Table 5). The more pronounced shift is probably the result of a stronger interaction

Table 5 Binding energy for $MAPbI_3$/fullerene films and calculated R_{ct} and R_{rec} for devices fabricated with the fullerene derivatives

	Binding energy (eV)		Resistance	
Compound	Pb 4f $_{7/2}$	Pb 4f $_{5/2}$	R_{ct} (Ω)	R_{rec} (Ω)
Perovskite	137.98	142.86		
Perovskite/$PC_{61}BM$	138.14	143.04	6972	21 561
Perovskite/BPy-C_{60}	138.40	143.28	4873	36 279
Perovskite/BpAn-C_{60}	137.84	142.69	6892	24 186
Perovskite/BAn-C_{60}	138.02	142.97	5927	31 862

of the pyridine residue with the perovskite layer, due to the enhanced basic character of the electrons in the pyridine nitrogen. The other compounds can also interact with the interfacial Pb^{2+} *via* carbonyl, carbamate or amino groups but these interactions are weaker.

Additionally, EIS measurements were conducted to gain insights into the electron extraction and transport processes at the interfaces (Fig. 7b). As shown in Fig. 7b and Table 5, all compounds showed a higher resistance to recombination (R_{rec}) and a smaller resistance to electron transfer (R_{ct}) compared to $PC_{61}BM$. This result supports the fact that the derivatives are efficient electron extraction materials at the interface, which is driven by the interfacial interaction with the surface of the perovskite and the ability of the fullerenes to passivate it.

Conclusions

In this work, we synthesized and characterized fullerene derivatives with functionalities that possess different basicities. The compounds were tested as ETMs and EELs in PSC devices using $PC_{61}BM$ and C_{60} as controls. The results showed that the compounds exhibited a rather limited performance when

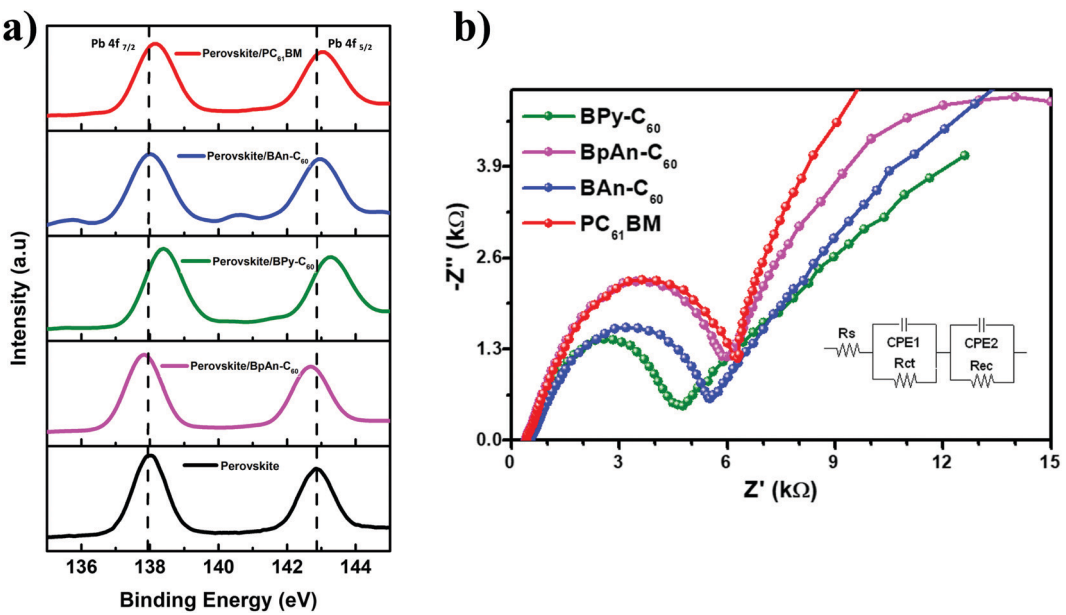

Fig. 7 (a) XPS measurements of the Pb 4f region for $MAPbI_3$/fullerene films and (b) EIS studies for devices fabricated with the as-synthesized fullerene derivatives.

employed as ETMs, however, by using them as EELs at the interface between the perovskite and C_{60} (ETL), we observed the dependence of the thickness of the fullerene layer with the overall photovoltaic performance. The results showed that the synthesized compounds are better at extracting the electrons at the surface of the perovskite but not at transporting them through the bulk of the layer ($\sim$85 nm) to the Ag electrode. SS-and TRPL measurements showed the improved ability of the compounds to passivate the perovskite layer and to extract the electrons from the interface due to interfacial interactions of the pyridine, aniline, carbonyl and carbamate groups with the uncoordinated Pb^{2+}. The XPS measurements revealed a stronger interaction of the BPy-C_{60} compound with the surface of the perovskite driven by the higher basicity of the pyridine group when compared to the other compounds. Additional EIS, conductivity and electron mobility measurements were performed, and the results indicated a reduced ability to transport electrons, an increased conductivity and a smaller resistance to electron transfer at the interface when compared to the devices used as controls. These results explain the better photovoltaic performance of BPy-C_{60} as EEL when used as a very thin layer, due to its intrinsic capability to extract electrons at the perovskite/fullerene interfaces. Conceptually, we introduce in this article the idea of subdividing the ETM into an EEL and ETL to study the electron extraction at the interface and transport of the electrons at the bulk separately to obtain the optimal conditions in each case, yielding better performing devices. This concept can be used in future work to design "the perfect" fullerene derivative that would be able to optimally extract electrons at the interface as well as to transport them to the Ag electrode.

Experimental section

General materials and methods

All chemicals were reagent grade. Silica gel (40–60 μ, 60 Å) was used to separate and purify the products. High resolution Mass Spectrometry (HRMS) experiments were performed using a Thermo Scientific Q-Exactive Oribtrap instrument equipped with a Dionex Ultimate 3000 (RSLC) inlet system, and electrospray (ESI) and atmospheric pressure chemical (APCI) ionization sources. CV experiments were performed under an argon atmosphere at room temperature. The scan rate for the CV experiments was 100 mV s^{-1}. A one compartment cell with a standard three-electrode configuration was used, consisting of a 1 mm diameter glassy carbon disk as the working electrode, a platinum wire as the counter electrode and a silver wire as a pseudo-reference electrode, in a solution of anhydrous *ortho*-dichlorobenzene (*o*-DCB) containing 0.05 M *n*-Bu_4NPF_6. Ferrocene was added to the solution at the end of each experiment as an internal standard.

The UV/Vis-NIR spectra were recorded for toluene solutions. The NMR spectra were recorded using a JEOL 600 MHz and a Bruker 400 MHz spectrometers.

Device fabrication

ITO-coated glass was purchased from Liaoning Huite Photoelectric Technology Co., Ltd. PbI_2 (99%) was bought from Sigma-Aldrich. $PC_{61}BM$ (99%) and C_{60} (99.8%) were purchased from SES Research. Methyl ammonium iodide (CH_3NH_3I, 99.5%) was bought from Greatcellsolar. The glasses for the fabrication of the devices were cut and etched with hydrochloric concentrated acid at boiling temperature. The cleaning process included 15 minutes of sonication with Alconox Detergent 8, followed by 15 minutes sonication with water, then isopropanol and acetone. Finally, the devices were dried with high purity nitrogen flow and left under UV–ozone treatment for 30 minutes. A solution of 25 mg of nickel acetate dihydrate in 1 mL of ethanol and 50 μL ethanolamine was prepared and stirred overnight. The resulting blue solution was filtered and spun onto the treated ITO substrates at 3000 rpm for 40 s and then heated at 350 °C for 30 min in air. The devices were transferred to a N_2-filled glovebox, where a previously prepared overnight solution of $CH_3NH_3PbI_3$ (1.2 M in DMF/DMSO, 7 : 3) was deposited on the NiO_x-coated substrates at 1000 rpm for 5 s and at 6000 rpm for 45 s. After 10 s, in the second step, 500 μL of toluene were dripped, and the corresponding films were annealed at 100 °C for 10 min. The fullerene derivatives previously dissolved in chlorobenzene (20 mg mL^{-1}) were spin-coated onto the perovskite layer at 1000 rpm for 60 s and annealed at 80 °C for 15 min. When the fullerene derivatives were applied as an interfacial layer between the perovskite and C_{60}, a spin rate of 2000 rpm for 40 s was used. Then, a solution of 1 mg mL^{-1} of BCP in ethanol was spun at 4000 rpm for 30 s. Finally, Ag electrodes (100 nm) were deposited by thermal evaporation under a pressure of 1×10^{-6} Torr through a shadow mask. The active area of the devices was 6 mm^2.

Device characterization

XRD measurements were done in a Panalytical Empyrean 2. Current–Voltage (*J*–*V*) characteristics of the devices and Space Charge Limited Current (SCLC) measurements were tested using a Keithley 2420 source meter under a Photo Emission Tech SS100 Solar Simulator, and the light intensity was calibrated by a standard Si solar cell. External quantum efficiencies (EQE) were measured using a Bentham (from Bentham Instruments Ltd) measurement system. The light intensity was calibrated using a single-crystal Si photovoltaic cell as the reference. The SEM images were collected using a ZEISS Sigma field-emission scanning electron microscope, where the electron beam was accelerated in the range of 500 V to 30 kV. The film thicknesses were measured using a KLA Tencor profilometer.

SS-PL measurements were performed using Fluorolog 3 spectrofluorimeter (Horiba Scientific) equipped with a visible photomultiplier tube (PMT) (220–800 nm, R928P; Hamamatsu), and a NIR PMT (950–1650 nm, H10330-75; Hamamatsu). All spectra were corrected for the instrumental functions.

The time-dependent decay of PL signals were measured using a MicroTime 200 time-resolved fluorescence microscope (PicoQuant), equipped with an inverted microscope setup (Olympus, IX73 inverted microscope) and a 405 nm excitation laser (MicroTime LDH-D-C-405). All optical measurements of the sample were conducted in a N_2 gas filled cell at room temperature.

XPS spectra were obtained using an ESCALAB 250XI XPS with a monochromated, microfocused Al Kα X-ray source at a spot size of 600 μm. Survey and high-resolution spectra were collected with a pass energy of 150 and 50 eV and a step size of 1.0 and 0.1 eV, respectively. All spectra were charge referenced to adventitious carbon (284.8 eV) and fitted using Thermo Scientific Avantage software.

EIS measurements were performed using a CH Instrument Electrochemical Station using a CHI660A electrochemical workstation software at 1 V in dark conditions. The increment was set to 0.05, the frequency from 0.1–100 000 Hz and the amplitude at 0.005.

Conflicts of interest

No conflicts of interest to declare.

Acknowledgements

The authors thank the US National Science Foundation (NSF) for generous support of this work under CHE-18001317 (to L. E.). The Robert A. Welch Foundation is also gratefully acknowledged for an endowed chair to L. E. (grant AH-0033). For use of the XRD instrument, the authors thank the DoD-HBCU Program (Grant No. 64705CHREP).

References

1 NREL, Best Research-Cell Efficiencies, https://www.nrel.gov/pv/assets/pdfs/best-research-cell-efficiencies.20200919.pdf, accessed accessed September, 2020, 2020.
2 H. S. Jung and N.-G. Park, *Small*, 2015, **11**, 10–25.
3 Z. Chen, Q. Dong, Y. Liu, C. Bao, Y. Fang, Y. Lin, S. Tang, Q. Wang, X. Xiao, Y. Bai, Y. Deng and J. Huang, *Nat. Commun.*, 2017, **8**, 1890.
4 K. Leng, I. Abdelwahab, I. Verzhbitskiy, M. Telychko, L. Chu, W. Fu, X. Chi, N. Guo, Z. Chen, Z. Chen, C. Zhang, Q.-H. Xu, J. Lu, M. Chhowalla, G. Eda and K. P. Loh, *Nat. Mater.*, 2018, **17**, 908–914.
5 X. He, Y. Qiu and S. Yang, *Adv. Mater.*, 2017, **29**, 1700775.
6 C. J. Bartel, J. M. Clary, C. Sutton, D. Vigil-Fowler, B. R. Goldsmith, A. M. Holder and C. B. Musgrave, *J. Am. Chem. Soc.*, 2020, **142**, 5135–5145.
7 F. Wang, S. Bai, W. Tress, A. Hagfeldt and F. Gao, *npj Flex. Electron.*, 2018, **2**, 22.
8 K. X. Steirer, P. Schulz, G. Teeter, V. Stevanovic, M. Yang, K. Zhu and J. J. Berry, *ACS Energy Lett.*, 2016, **1**, 360–366.
9 Q. Dong, Y. Fang, Y. Shao, P. Mulligan, J. Qiu, L. Cao and J. Huang, *Science*, 2015, **347**, 967–970.
10 W. Ning, F. Wang, B. Wu, J. Lu, Z. Yan, X. Liu, Y. Tao, J.-M. Liu, W. Huang, M. Fahlman, L. Hultman, T. C. Sum and F. Gao, *Adv. Mater.*, 2018, **30**, 1706246.
11 S. Bai, Z. Wu, X. Wu, Y. Jin, N. Zhao, Z. Chen, Q. Mei, X. Wang, Z. Ye, T. Song, R. Liu, S.-T. Lee and B. Sun, *Nano Res.*, 2014, **7**, 1749–1758.
12 S. Magazine, Types of Solar Panels: On the Market and in the Lab [2020], https://solarmagazine.com/solar-panels/, accessed November 2020, 2020.
13 *Nature*, 2019, **570**, 429–432, DOI: 10.1038/d41586-019-01985-y.
14 J. M. Ball and A. Petrozza, *Nat. Energy*, 2016, **1**, 16149.
15 C. Liu, Z. Huang, X. Hu, X. Meng, L. Huang, J. Xiong, L. Tan and Y. Chen, *ACS Appl. Mater. Interfaces*, 2018, **10**, 1909–1916.
16 F. Gao, Y. Zhao, X. Zhang and J. You, *Adv. Energy Mater.*, 2020, **10**, 1902650.
17 O. Fernandez-Delgado, E. Castro, C. R. Ganivet, K. Fosnacht, F. Liu, T. Mates, Y. Liu, X. Wu and L. Echegoyen, *ACS Appl. Mater. Interfaces*, 2019, **11**, 34408–34415.
18 E. Castro, J. Murillo, O. Fernandez-Delgado and L. Echegoyen, *J. Mater. Chem. C*, 2018, **6**, 2635–2651.
19 E. Castro, O. Fernandez-Delgado, F. Arslan, G. Zavala, T. Yang, S. Seetharaman, F. D'Souza and L. Echegoyen, *New J. Chem.*, 2018, **42**, 14551–14558.
20 J. Xiao, J. Shi, D. Li and Q. Meng, *Sci. China: Chem.*, 2015, **58**, 221–238.
21 C. Xu, Z. Liu and E.-C. Lee, *J. Mater. Chem. C*, 2018, **6**, 6975–6981.
22 A. Mei, X. Li, L. Liu, Z. Ku, T. Liu, Y. Rong, M. Xu, M. Hu, J. Chen, Y. Yang, M. Grätzel and H. Han, *Science*, 2014, **345**, 295–298.
23 X. Liu, H. Yu, L. Yan, Q. Dong, Q. Wan, Y. Zhou, B. Song and Y. Li, *ACS Appl. Mater. Interfaces*, 2015, **7**, 6230–6237.
24 J. You, L. Meng, T.-B. Song, T.-F. Guo, Y. Yang, W.-H. Chang, Z. Hong, H. Chen, H. Zhou, Q. Chen, Y. Liu, N. De Marco and Y. Yang, *Nat. Nanotechnol.*, 2016, **11**, 75–81.
25 C.-Y. Chang, W.-K. Huang, Y.-C. Chang, K.-T. Lee and C.-T. Chen, *J. Mater. Chem. A*, 2016, **4**, 640–648.
26 C. M. Wolff, F. Zu, A. Paulke, L. P. Toro, N. Koch and D. Neher, *Adv. Mater.*, 2017, **29**, 1700159.
27 J. Y. Jeng, Y. F. Chiang, M. H. Lee, S. R. Peng, T. F. Guo, P. Chen and T. C. Wen, *Adv. Mater.*, 2013, **25**, 3727–3732.
28 Z. Xiao, C. Bi, Y. Shao, Q. Dong, Q. Wang, Y. Yuan, C. Wang, Y. Gao and J. Huang, *Energy Environ. Sci.*, 2014, **7**, 2619–2623.
29 P.-W. Liang, C.-Y. Liao, C.-C. Chueh, F. Zuo, S. T. Williams, X.-K. Xin, J. Lin and A. K.-Y. Jen, *Adv. Mater.*, 2014, **26**, 3748–3754.
30 J. Xie, V. Arivazhagan, K. Xiao, K. Yan, Z. Yang, Y. Qiang, P. Hang, G. Li, C. Cui, X. Yu and D. Yang, *J. Mater. Chem. A*, 2018, **6**, 5566–5573.
31 J. Seo, S. Park, Y. Chan Kim, N. J. Jeon, J. H. Noh, S. C. Yoon and S. I. Seok, *Energy Environ. Sci.*, 2014, **7**, 2642–2646.
32 C.-H. Chiang, Z.-L. Tseng and C.-G. Wu, *J. Mater. Chem. A*, 2014, **2**, 15897–15903.
33 H. Zhang, H. Azimi, Y. Hou, T. Ameri, T. Przybilla, E. Spiecker, M. Kraft, U. Scherf and C. J. Brabec, *Chem. Mater.*, 2014, **26**, 5190–5193.
34 J. H. Kim, P. W. Liang, S. T. Williams, N. Cho, C. C. Chueh, M. S. Glaz, D. S. Ginger and A. K. Jen, *Adv. Mater.*, 2015, **27**, 695–701.
35 H. Azimi, T. Ameri, H. Zhang, Y. Hou, C. O. R. Quiroz, J. Min, M. Hu, Z.-G. Zhang, T. Przybilla, G. J. Matt, E. Spiecker, Y. Li and C. J. Brabec, *Adv. Energy Mater.*, 2015, **5**, 1401692.

36 W. Li, H. Wang, X. Hu, W. Cai, C. Zhang, M. Wang and Z. Zang, *Solar RRL*, 2021, **5**, 2000573.
37 M. Wang, H. Wang, W. Li, X. Hu, K. Sun and Z. Zang, *J. Mater. Chem. A*, 2019, **7**, 26421–26428.
38 M. Wang, Z. Zang, B. Yang, X. Hu, K. Sun and L. Sun, *Solar Energy Mater. Solar Cells*, 2018, **185**, 117–123.
39 X. Hu, H. Wang, Y. Ying, M. Wang, C. Zhang, Y. Ding, H. Li, W. Li, S. Zhao and Z. Zang, *J. Power Sources*, 2020, **480**, 229073.
40 X. Liu, P. Li, Y. Zhang, X. Hu, Y. Duan, F. Li, D. Li, G. Shao and Y. Song, *J. Power Sources*, 2019, **413**, 459–466.
41 A.-N. Cho and N.-G. Park, *ChemSusChem*, 2017, **10**, 3687–3704.
42 I. Grill, M. F. Aygüler, T. Bein, P. Docampo, N. F. Hartmann, M. Handloser and A. Hartschuh, *ACS Appl. Mater. Interfaces*, 2017, **9**, 37655–37661.
43 W. Reusch, Text of Organic Chemistry 1999, https://www2.chemistry.msu.edu/faculty/reusch/VirtTxtJml/intro1.htm.
44 T. Soderberg, *Journal*, 2016, 468.
45 D. E. Williams, E. A. Dolgopolova, D. C. Godfrey, E. D. Ermolaeva, P. J. Pellechia, A. B. Greytak, M. D. Smith, S. M. Avdoshenko, A. A. Popov and N. B. Shustova, *Angew. Chem., Int. Ed.*, 2016, **55**, 9070–9074.
46 O. Fernandez-Delgado, E. Castro, C. R. Ganivet, K. Fosnacht, F. Liu, T. Mates, Y. Liu, X. Wu and L. Echegoyen, *ACS Appl. Mater. Interfaces*, 2019, **11**, 34408–34415.
47 J. C. S. Costa, R. J. S. Taveira, C. F. R. A. C. Lima, A. Mendes and L. M. N. B. F. Santos, *Opt. Mater.*, 2016, **58**, 51–60.
48 W.-Y. Chen, L.-L. Deng, S.-M. Dai, X. Wang, C.-B. Tian, X.-X. Zhan, S.-Y. Xie, R.-B. Huang and L.-S. Zheng, *J. Mater. Chem. A*, 2015, **3**, 19353–19359.